

<sub>1</sub> Physics-Infused Reduced-Order Modeling for Analysis of  
<sub>2</sub> Ablating Hypersonic Thermal Protection Systems

<sub>3</sub>

<sub>4</sub> October 27, 2025

<sub>5</sub> **Abstract**

<sub>6</sub> This work presents a physics-infused reduced-order modeling (PIROM) framework  
<sub>7</sub> towards the design, analysis, and optimization of non-decomposing ablating hypersonic  
<sub>8</sub> thermal protection systems (TPS).

<sub>9</sub> **1 Introduction**

<sub>10</sub> At hypersonic speeds, aerospace vehicles experience extreme aero-thermal environments that  
<sub>11</sub> requires specialized thermal protection systems (TPS) to shield internal sub-structures, elec-  
<sub>12</sub> tronics, and possibly crew members from the intense aerodynamic heating. The TPS is often  
<sub>13</sub> composed of ablating materials – a high-temperature capable fibrous material injected with  
<sub>14</sub> a resin that fills the pore network and strengthens the composite [Amar2016](#). The TPS de-  
<sub>15</sub> sign promotes the exchange of mass through thermal and chemical reactions (i.e., pyrolysis),  
<sub>16</sub> effectively mitigating heat transfer to the sub-structures.

<sub>17</sub> As a result, accurate prediction for the ablating TPS response under extreme hypersonic  
<sub>18</sub> heating becomes fundamental to ensuring survivability, performance, and safety of hyper-  
<sub>19</sub> sonic vehicles. Not only is it necessary to assess the performance of the thermal management  
<sub>20</sub> systems, but also the shape changes of the vehicle’s outer surface induced by the ablating  
<sub>21</sub> material, and its impact on the aerodynamics, structural integrity, and controllability. Un-  
<sub>22</sub> fortunately, high-fidelity simulations of ablating TPS remains a formidable challenge both  
<sub>23</sub> theoretically and computationally.

<sub>24</sub> On the theoretical side, the thermo-chemical reactions, coupled with the irregular pore  
<sub>25</sub> network structure, translate into simplifying assumptions to reduce non-linearities, and make  
<sub>26</sub> the resulting equations more amenable for engineering application and design analysis [x](#).  
<sub>27</sub> For instance, one of the most notable codes is the one-dimensional [CMA](#) code that was

28 developed by Aerotherm Corporation in the 1960s [Howard2015](#). Despite its practical use  
29 in...

30 Another example is the CHarring Ablator Response (CHAR) ablation code, which ignores  
31 elemental decompositions of the pyrolyzing gases, assumes the gases to be a mixture of perfect  
32 gases in thermal equilibrium, and assumes no reaction or condensation with the porous  
33 network [?].

34 theoretically:

35 computationally:

## 36 2 Modeling of Ablating Thermal Protection Systems

37 This section presents the problem of modeling ablation for a non-decomposing TPS as a  
38 parametrized system of coupled non-linear PDEs. The ablation physics is decomposed into  
39 heat conduction and mesh motion, which are governed by the energy and pseudo-elasticity  
40 PDEs, respectively. Predictions for the ablating TPS response computed based on two  
41 models: (1) a high-fidelity FOM based on discontinuous Galerkin FEM (DG-FEM), and (2)  
42 an RPM based on the LCM. The mathematical details for the governing equations, FOM,  
43 and RPM, are provided next.

### 44 2.1 Governing Equations

45 **Heat Conduction** Consider a generic domain  $\Omega \subset \mathbb{R}^d$ ,  $d = 2$  or  $3$ , illustrated in Fig. 1. Let  
46  $\partial\Omega = \Gamma_q \cup \Gamma_T$  and  $\Gamma_q \cap \Gamma_T = \emptyset$ , where a Neumann  $q_b(x, t)$  boundary condition is prescribed on  
47 the  $\Gamma_q$  boundary, and a Dirichlet  $T_b(x, t)$  boundary condition is prescribed on the boundary  
48  $\Gamma_T$ . The ablation is modeled as mesh motion, and occurs only on the heated boundary  $\Gamma_q$ .  
49 Ablating effects on the energy equation are handled using the Arbitrary Lagrangian-Eulerian  
50 (ALE) description. The ALE establishes that mesh displacements  $w(x, t) \in \mathbb{R}^d$  and velocities  
51  $v(x, t) \in \mathbb{R}^d$  evolve independently of the physical material's displacements, which are set to  
52 zero [CITE](#).

53 The transient heat conduction is described by the energy equation,

$$54 \rho c_p \left( \frac{\partial T}{\partial t} - v(x, t) \cdot \nabla T \right) - \nabla \cdot (\mathbf{k} \nabla T) = \mathcal{Q}(x, t), \quad x \in \Omega \quad (1a)$$

$$55 -\mathbf{k} \nabla T \cdot \mathbf{n} = q_b(x, t), \quad x \in \Gamma_q \quad (1b)$$

$$56 T(x, t) = T_b(x, t), \quad x \in \Gamma_T \quad (1c)$$

$$57 T(x, 0) = T_0(x), \quad x \in \Omega \quad (1d)$$

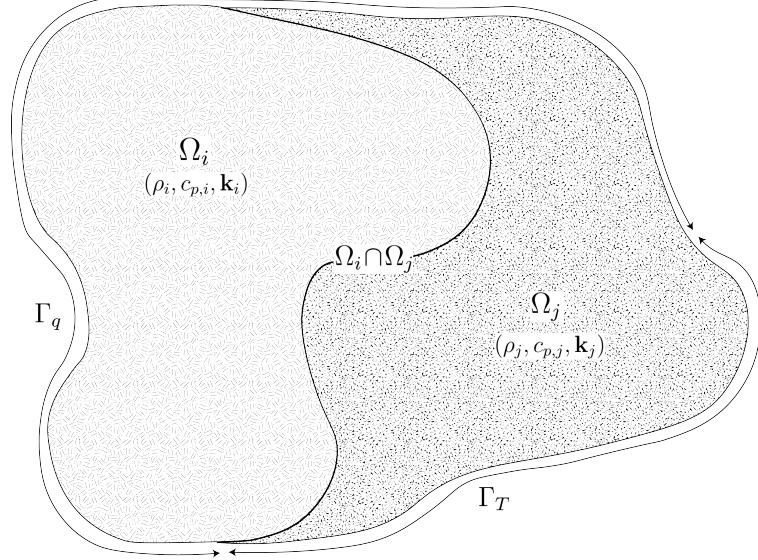


Figure 1: General domain  $\Omega$  with prescribed Neumann and Dirichlet boundary conditions on  $\Gamma_q$  and  $\Gamma_T$ . Mesh displacement  $w(x, t)$  occurs on the  $\Gamma_q$  boundary.

where the density  $\rho$  is constant, while the heat capacity  $c_p$  and thermal conductivity  $\mathbf{k} \in \mathbb{R}^{d \times d}$ , are temperature dependent. In the order they appear, the terms in eq. (1a) include, the unsteady energy storage, heat conduction, temperature advection due to mesh motion, and source terms due to boundary conditions. The boundary conditions for the energy equation includes Neumann eq. (1b) on  $\Gamma_1$  and Dirichlet eq. (1c) on  $\Gamma_T$ .

**Mesh Motion** The mesh motion is described by the pseudo-elasticity equation,

$$\nabla \cdot \sigma(w) = 0 \quad (2a)$$

$$w(x, t) = w_q(x, t), \quad x \in \Gamma_q \quad (2b)$$

$$w(x, t) = 0, \quad x \notin \Gamma_q \quad (2c)$$

$$w(x, 0) = \mathbf{0} \quad (2d)$$

where the stress tensor  $\sigma$  is related to the strain tensor  $\epsilon(w)$  through Hooke's law,

$$\sigma(w) = \mathbb{D} : \epsilon(w)$$

where  $\mathbb{D}$  is the constitutive operator, “ $:$ ” is the double contraction of tensors, and  $\epsilon$  is the symmetric strain tensor given by,

$$\epsilon(\mathbf{w}) = \frac{1}{2} (\nabla \mathbf{w} + \nabla \mathbf{w}^T)$$

63 The “material” properties for the mesh are chosen to tailor the mesh deformation, and need  
 64 not represent the actual material being modeled Amar2016.

65 For the pseudo-elasticity equations, the surface velocity due to the ablating material is a  
 66 function of the surface temperature  $T_q(x, t)$  for  $x \in \Gamma_q$  on the heated boundary. For the  $i$ -th  
 67 material component, the surface velocity is imposed based on the following relation,

$$\hat{\mathbf{n}} \cdot \mathbf{v}(x, t) = f(T_q(x, t)), \quad x \in \Gamma_q \quad (3)$$

68 where  $\hat{\mathbf{n}}$  is the unit normal vector on the heated boundary  $\Gamma_q$ , and  $f$  is a function obtained  
 69 from tabulated data for the material, commonly referred to as a B’ table. The B’ table  
 70 provides the recession velocity as a function of surface temperature, and is pre-computed  
 71 based on high-fidelity simulations of the ablation process for a one-dimensional slab of the  
 72 material, and is independent of the TPS geometry and boundary conditions. The surface  
 73 displacements are then computed by integrating the surface velocities over time,

$$\mathbf{w}_q(x, t) = \int_0^t \mathbf{v}(x, \tau) d\tau = \int_0^t f(T_q(x, \tau)) d\tau \quad (4)$$

## 74 2.2 Full-Order Model: Finite-Element Method

75 To obtain the full-order numerical solution, the governing equation is spatially discretized  
 76 using variational principles of Discontinuous Galerkin (DG) to result in a high-dimensional  
 77 system of ordinary differential equations (ODEs). Note that the choice of DG approach here  
 78 is mainly for theoretical convenience in the coarse-graining formulation, and is exclusively  
 79 performed on the energy equation as the quantities of interest correspond to the ablating  
 80 surface temperatures. In Sec. x, the high-fidelity ablating TPS solution is performed using  
 81 standard FEM for both the energy and elasticitiy equations, and the equivalence between  
 82 DG and standard FEM is noted upon their convergence.

83 Consider a conforming mesh partition domain, where each element belongs to one and  
 84 only one component. Denote the collection of all  $M$  elements as  $\{E_i\}_{i=1}^M$ . In an element  $E_i$ ,  
 85 its shared boundaries with another element  $E_j$ , Neumann BC, and Dirichlet BC are denoted  
 86 as  $e_{ij}$ ,  $e_{iq}$ , and  $e_{iT}$ , respectively. Lastly,  $|e|$  denotes the length ( $n_d = 2$ ) or area ( $n_d = 3$ ) of a  
 87 component boundary  $e$ .

88 For the  $i$ -th element, use a set of  $P$  trial functions, such as polynomials, to represent the  
 89 temperature distribution,

$$T^{(i)}(x, t) = \sum_{l=1}^P \phi_l^{(i)}(x) u_l^{(i)} \equiv \boldsymbol{\phi}^{(i)}(x)^T \mathbf{u}^{(i)}(t), \quad i = 1, 2, \dots, M \quad (5)$$

90 By standard variational processes, e.g., Cohen2018, the element-wise governing equation is  
 91 denoted as,

$$\mathbf{A}^{(i)} \dot{\mathbf{u}}^{(i)} = (\mathbf{B}^{(i)} + \mathbf{C}^{(i)}) \mathbf{u}^{(i)} + \sum_{j \in \mathcal{N}_i \cup \{T_b\}} \left( \mathbf{B}_{ij}^{(i)} \mathbf{u}^{(i)} + \mathbf{B}_{ij}^{(j)} \mathbf{u}^{(j)} \right) + \mathbf{f}^{(i)}(t), \quad \text{for } i = 1, 2, \dots, M \quad (6)$$

92 which is collected as the following ODE for all the elements in the mesh,

$$\mathbf{A}(\mathbf{u}) \dot{\mathbf{u}} = [\mathbf{B}(\mathbf{u}) + \mathbf{C}(\mathbf{u})] \mathbf{u} + \mathbf{f}(t) \quad (7)$$

93 where  $\mathbf{u} = [\mathbf{u}^{(1)}, \mathbf{u}^{(2)}, \dots, \mathbf{u}^{(M)}]^T \in \mathbb{R}^{MP}$  includes all the DG variables,  $\mathbf{f} \in \mathbb{R}^{MP}$  is the  
 94 external forcing, and the system matrices  $\mathbf{A}$ ,  $\mathbf{B}$ , and  $\mathbf{C}$  are the matrices due to heat capacity,  
 95 heat conduction, and temperature advection due to mesh motion, respectively. A detailed  
 96 derivation of eqs. (6) and (7) and their matrices is provided in Appendix [?].

## 97 2.3 Reduced-Physics Model

98 The RPM for predicting the response of the ablating TPS consists of two components: (1) the  
 99 LCM, and (2) tabulated data for ablating velocity as a function of surface temperature. The  
 100 LCM is described as a first-order system of ODEs for predicting the average temperatures  
 101 inside the ablating TPS, and provides a low-fidelity under-estimation for the ablating surface  
 102 temperature. The temperature prediction from LCM is used in a B' table to determine the  
 103 surface recession velocity, from which the displacements are obtained through integration.

### 104 2.3.1 Lumped Capacitance Model

105 The main results regarding the LCM are provided in this section; details of the implementa-  
 106 tion for the TPS in Fig. 2 are provided in Appendix A. The LCM is a classical physics-based  
 107 low-order model for predicting the temporal variation of average temperature in multiple in-  
 108 terconnected components INCROPERA. The LCM is derived at the component level from  
 109 a point of view of energy conservation, and leads to the following system of ODEs for the  
 110 average temperatures on the components,

$$\bar{\mathbf{A}} \dot{\bar{\mathbf{u}}} = \bar{\mathbf{B}}(\bar{\mathbf{u}}) \bar{\mathbf{u}} + \bar{\mathbf{f}}(t) \quad (8)$$

111 where,

$$\bar{\mathbf{u}} = [\bar{u}^{(1)}, \bar{u}^{(2)}, \dots, \bar{u}^{(N)}]^T \in \mathbb{R}^N \quad (9a)$$

$$\bar{\mathbf{f}} = [\bar{f}^{(1)}, \bar{f}^{(2)}, \dots, \bar{f}^{(N)}]^T \in \mathbb{R}^N \quad (9b)$$

112 includes the average temperatures  $\bar{\mathbf{u}}$  and forcing inputs  $\bar{\mathbf{f}}$  for the  $N$  components. For  $i, j =$   
113  $1, 2, \dots, N$  the  $(i, j)$ -th elements of the  $\bar{\mathbf{A}} \in \mathbb{R}^{N \times N}$ ,  $\bar{\mathbf{B}} \in \mathbb{R}^{N \times N}$ , and  $\bar{\mathbf{f}} \in \mathbb{R}^N$  matrices are  
114 given by,

$$\bar{A}^{(i)} = \begin{cases} \int_{\Omega^{(i)}} \rho c_p d\Omega^{(i)}, & i = j \\ 0, & i \neq j \end{cases}, \quad \bar{B}_{ij} = \begin{cases} \sum_{j \in \mathcal{N}_i \cup \{T_b\}} \bar{B}_{ij}^{(i)}, & i = j \\ \bar{B}_{ij}^{(j)}, & i \neq j \end{cases}, \quad (10a)$$

$$\mathbf{f}^{(i)} = \begin{cases} |e_{iq}| \bar{q}^{(i)} + \frac{|e_{iT}|}{R_i} \bar{T}^{(i)}, & i = j \\ 0, & i \neq j \end{cases} \quad (10b)$$

115 where,

$$\bar{q}^{(i)} = \frac{1}{|e_{iq}|} \int_{e_{iq}} q_b de_{iq}, \quad \bar{T}^{(i)} = \frac{1}{|e_{iT}|} \int_{e_{iT}} T_b de_{iT}, \quad \bar{B}_{ij}^{(i)} = -\frac{|e_{ij}|}{R_{ij}}, \quad \bar{B}_{ij}^{(j)} = \frac{|e_{ij}|}{R_{ij}} \quad (11)$$

### 116 2.3.2 Surface Recession Velocity and Displacements

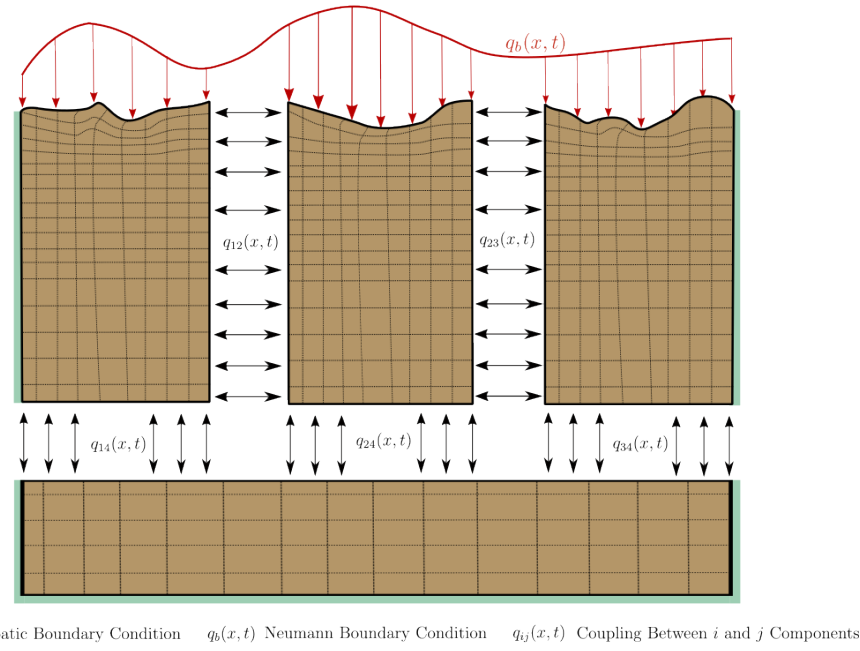
117 The surface velocity on the heated boundary  $\Gamma_q$  is computed based on the temperature  
118 predicted by the LCM using eq. (3). Thus, based on the  $i$ -th average temperature  $\bar{u}^{(i)}$ , the  
119 wall-normal surface velocity is computed as,

$$\hat{\mathbf{n}} \cdot \mathbf{v}^{(i)}(x, t) = f(\bar{u}^{(i)}(t)) \quad (12)$$

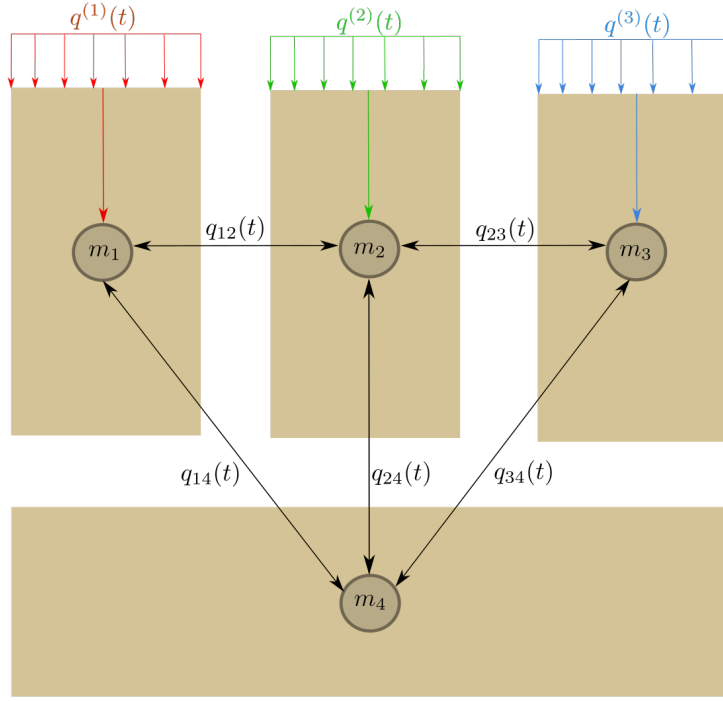
120 Due

## 121 2.4 Summary of Modeling Approaches

122 The FOM (i.e., DG-FEM) and RPM (i.e., LCM) are two different but mathematically con-  
123 nected solution strategies. Specifically, the LCM in eq. (8) not only resembles the functional  
124 form of the DG model in eq. (7), but can be viewed as a special case of the latter, where the  
125 mesh partition is extremely coarse, and the trial and test functions are piece-wise constants.  
126 For example, consider the case where each component  $\Omega^{(i)}$  is treated as one single element,  
127 and each element employs one constant basis function  $\phi^{(i)} = 1$ . The element-wise DG model



(a) TPS Decomposition



(b) Lumped Mass Representation

Figure 2: Partition of the TPS into three ablating and one non-ablating components with the corresponding lumped-mass representation.

128 in eq. (6) simplifies into a scalar ODE that ignores advection effects due to mesh motion,

$$\mathbf{A}^{(i)} = \bar{A}^{(i)}, \quad \mathbf{C}^{(i)} = 0, \quad \mathbf{B}_{ij}^{(i)} = -\sigma|e_{ij}|, \quad \mathbf{B}_{ij}^{(j)} = \sigma|e_{ij}|, \quad \mathbf{f}^{(i)} = |e_{iq}|\bar{q}^{(i)} + \sigma|e_{iT}|\bar{T}^{(i)} \quad (13)$$

129 Clearly, the LCM is a coarse zeroth-order DG model with the inverse of thermal resistance  
130 chosen as the element-wise penalty factors. Or conversely, the DG model is a refined version  
131 of LCM via *hp*-adaptation.

132 The FOM and RPM represent two extremes in the modeling fidelity and computational  
133 cost spectrum. On one hand, the FOM is the most accurate but computationally expensive  
134 to evaluate due to the fine mesh discretizations for both the temperature and displacement  
135 fields, leading to possibly millions of state variables. On the other hand, the RPM considers  
136 only the average temperature of the material as the state variable, considerably reducing  
137 the computational cost, but sacrificing local temperature information and thus neglecting  
138 higher-order effects due to mesh motion. Thus, neither the FOM nor the RPM is a universal  
139 approach for real-world analysis, design, and optimization tasks for ablating TPS, where  
140 thousands of high-fidelity model evaluations may be necessary. This issue motivates the  
141 development of the PIROM, which can achieve the fidelity of FOM at a computational cost  
142 close to the RPM, while maintaining the generalizability to model parameters.

### 143 3 Physics-Infused Reduced-Order Modeling

144 The formulation of PIROM for ablating TPS starts by connecting the FOM, i.e., DG-FEM,  
145 and the RPM, i.e., the LCM, via a coarse-graining procedure. This procedure pinpoints  
146 the missing dynamics in the LCM when compared to DG-FEM. Subsequently, the Mori-  
147 Zwanzig (MZ) formalism is employed to determine the model form for the missing dynamics  
148 in PIROM. Lastly, the data-driven identification of the missing dynamics in PIROM is  
149 presented.

#### 150 3.1 Deriving the Reduced-Physics Model via Coarse-Graining

151 The LCM is derived from a full-order DG on a fine mesh via coarse graining. This pro-  
152 cess constraints the trial function space of a full-order DG model to a subset of piece-wise  
153 constants, so that the variables  $\mathbf{u}$ , matrices  $\mathbf{A}$ ,  $\mathbf{B}$ , and  $\mathbf{C}$ , and forcing vector  $\mathbf{f}$  are all ap-  
154 proximated using a single state associated to the average temperature. The details of the  
155 projection are described next.

<sup>156</sup> **3.1.1 Coarse-Graining of States**

<sup>157</sup> Consider a DG model as in eq. (7) for  $M$  elements and an LCM as in eq. (8) for  $N$  components;  
<sup>158</sup> clearly  $M \gg N$ . Let  $\mathcal{V}_j = \{i | E_i \in \Omega_j\}$  be the indices of the elements belonging to the  $j$ -th  
<sup>159</sup> component, so  $E_i \in \Omega_j$  for all  $i \in \mathcal{V}_j$ . The number of elements in the  $j$ -th component is  $|\mathcal{V}_j|$ .  
<sup>160</sup> The average temperature on  $\Omega_j$  is,

$$\bar{u}_j = \frac{1}{|\Omega_j|} \sum_{i \in \mathcal{V}_j} \int_{E^{(i)}} \phi^{(i)}(x)^T \mathbf{u}^{(i)} d\Omega = \frac{1}{|\Omega_j|} \sum_{i \in \mathcal{V}_j} |E_i| \boldsymbol{\varphi}_i^{j\top} \mathbf{u}^{(i)}, \quad j = 1, 2, \dots, N \quad (14)$$

<sup>161</sup> where  $|\Omega_j|$  and  $|E_i|$  denote the area ( $d = 2$ ) or volume ( $d = 3$ ) of component  $j$  and element  
<sup>162</sup>  $i$ , respectively. The orthogonal basis functions are defined as  $\boldsymbol{\varphi}_i^{j\top} = [1, 0, \dots, 0]^\top \in \mathbb{R}^P$ .

<sup>163</sup> Conversely, given the average temperatures of the  $N$  components,  $\bar{\mathbf{u}}$ , the states of an  
<sup>164</sup> arbitrary element  $E_i$  is written as,

$$\mathbf{u}^{(i)} = \sum_{k=1}^N \boldsymbol{\varphi}_i^k \bar{u}_k + \delta \mathbf{u}^{(i)}, \quad i = 1, 2, \dots, M \quad (15)$$

<sup>165</sup> where  $\boldsymbol{\varphi}_i^k = 0$  if  $i \notin \mathcal{V}_k$ , and  $\delta \mathbf{u}^{(i)}$  represents the deviation from the average temperature and  
<sup>166</sup> satisfies the orthogonality condition  $\boldsymbol{\varphi}_i^{k\top} \delta \mathbf{u}^{(i)} = 0$  for all  $k$ .

<sup>167</sup> Equations eqs. (14) and (15) are combined and written in matrix form as,

$$\bar{\mathbf{u}} = \Phi^+ \mathbf{u}, \quad \mathbf{u} = \Phi \mathbf{u} + \delta \mathbf{u} \quad (16)$$

<sup>168</sup> where  $\Phi \in \mathbb{R}^{MP \times N}$  is a matrix of  $M \times N$  blocks, with the  $(i, j)$ -th block as  $\boldsymbol{\varphi}_i^j$ ,  $\Phi^+ \in \mathbb{R}^{N \times MP}$   
<sup>169</sup> is the left inverse of  $\Phi$ , with the  $(i, j)$ -th block as  $\boldsymbol{\varphi}_i^{j+} = \frac{|E_i|}{|\Omega_j|} \boldsymbol{\varphi}_i^{j\top}$ , and  $\delta \mathbf{u}$  is the collection of  
<sup>170</sup> deviations. By their definitions,  $\Phi^+ \Phi = \mathbf{I}$  and  $\Phi^+ \delta \mathbf{u} = \mathbf{0}$ .

<sup>171</sup> **3.1.2 Coarse-Graining of Dynamics**

<sup>172</sup> Next, consider a function of states in the form of  $\mathbf{M}(\mathbf{u}) \mathbf{g}(\mathbf{u})$ , where  $\mathbf{g} : \mathbb{R}^{MP} \rightarrow \mathbb{R}^{MP}$   
<sup>173</sup> is a vector-valued function, and  $\mathbf{M} : \mathbb{R}^{MP} \rightarrow \mathbb{R}^{p \times MP}$  is a matrix-valued function with an  
<sup>174</sup> arbitrary dimension  $p$ . Define the projection matrix  $\mathbf{P} = \Phi \Phi^+$  and the projection operator  
<sup>175</sup>  $\mathcal{P}$  as,

$$\begin{aligned} \mathcal{P} [\mathbf{M}(\mathbf{u}) \mathbf{g}(\mathbf{u})] &= \mathbf{M}(\mathbf{P} \mathbf{u}) \mathbf{g}(\mathbf{P} \mathbf{u}) \\ &= \mathbf{M}(\Phi \bar{\mathbf{u}}) \mathbf{g}(\Phi \bar{\mathbf{u}}) \end{aligned} \quad (17)$$

<sup>176</sup> so that the resulting function depends only on the average temperatures  $\bar{\mathbf{u}}$ . Correspondingly,  
<sup>177</sup> the residual operator  $\mathcal{Q} = \mathcal{I} - \mathcal{P}$ , and  $\mathcal{Q}[\mathbf{M}(\mathbf{u})\mathbf{g}(\mathbf{u})] = \mathbf{M}(\mathbf{u})\mathbf{g}(\mathbf{u}) - \mathbf{M}(\Phi\bar{\mathbf{u}})\mathbf{g}(\Phi\bar{\mathbf{u}})$ . When  
<sup>178</sup> the function is not separable, the projection operator is simply defined as  $\mathcal{P}[\mathbf{g}(\mathbf{u})] = \mathbf{g}(\mathbf{P}\mathbf{u})$ .

<sup>179</sup> Subsequently, the operators defined above are applied to coarse-grain the dynamics. First,  
<sup>180</sup> write the DG-FEM in eq. (7) as,

$$\dot{\mathbf{u}} = \mathbf{A}(\mathbf{u})^{-1}\mathbf{B}(\mathbf{u})\mathbf{u} + \mathbf{A}(\mathbf{u})^{-1}\mathbf{C}(\mathbf{u})\mathbf{u} + \mathbf{A}(\mathbf{u})^{-1}\mathbf{f}(t) \quad (18)$$

<sup>181</sup> and multiply both sides by  $\Phi^+$  to obtain,

$$\Phi^+\dot{\mathbf{u}} = \Phi^+(\Phi\dot{\bar{\mathbf{u}}} + \delta\dot{\mathbf{u}}) = \dot{\bar{\mathbf{u}}} = \Phi^+\mathbf{r}(\mathbf{u}, t) \quad (19)$$

<sup>182</sup> Apply the projection operator  $\mathcal{P}$  and the residual operator  $\mathcal{Q}$  to the right-hand side to obtain,

$$\dot{\bar{\mathbf{u}}} = \mathcal{P}[\Phi^+\mathbf{r}(\mathbf{u}, t)] + \mathcal{Q}[\Phi^+\mathbf{r}(\mathbf{u}, t)] \equiv \mathbf{r}^{(1)}(\mathbf{u}, t) + \mathbf{r}^{(2)}(\mathbf{u}, t) \quad (20)$$

<sup>183</sup> where  $\mathbf{r}^{(1)}(\mathbf{u}, t)$  is resolved dynamics that depends on  $\bar{\mathbf{u}}$  only, and  $\mathbf{r}^{(2)}(\mathbf{u}, t)$  is the un-resolved  
<sup>184</sup> or residual dynamics. Detailed derivations and analysis of  $\mathbf{r}^{(1)}(\mathbf{u}, t)$  and  $\mathbf{r}^{(2)}(\mathbf{u}, t)$  can be  
<sup>185</sup> found in the Appendix.

<sup>186</sup> It follows from Ref. [x](#) that the resolved dynamics is exactly the LCM, where the advection  
<sup>187</sup> term reduces to zero, i.e.,  $\bar{\mathbf{C}}(\bar{\mathbf{u}}) = \mathbf{0}$  as shown in the Appendix. Using the notation from  
<sup>188</sup> eq. (8), it follows that,

$$\begin{aligned} \mathbf{r}^{(1)}(\mathbf{u}, t) &= \bar{\mathbf{A}}(\bar{\mathbf{u}})^{-1}\bar{\mathbf{B}}(\bar{\mathbf{u}})\bar{\mathbf{u}} + \bar{\mathbf{A}}(\bar{\mathbf{u}})^{-1}\bar{\mathbf{C}}(\bar{\mathbf{u}})\bar{\mathbf{u}} + \bar{\mathbf{A}}(\bar{\mathbf{u}})^{-1}\bar{\mathbf{f}}(\bar{\mathbf{u}}) \\ &= \bar{\mathbf{A}}(\bar{\mathbf{u}})^{-1}\bar{\mathbf{B}}(\bar{\mathbf{u}})\bar{\mathbf{u}} + \bar{\mathbf{A}}(\bar{\mathbf{u}})^{-1}\bar{\mathbf{f}}(t) \end{aligned} \quad (21)$$

<sup>189</sup> where the following relations hold,

$$\bar{\mathbf{A}}(\bar{\mathbf{u}}) = \mathbf{W}(\Phi^+\mathbf{A}(\Phi\bar{\mathbf{u}})^{-1}\Phi)^{-1} \quad \bar{\mathbf{C}}(\bar{\mathbf{u}}) = \mathbf{0} \quad (22a)$$

$$\bar{\mathbf{B}}(\bar{\mathbf{u}}) = \mathbf{W}\Phi^+\mathbf{B}(\Phi\bar{\mathbf{u}})\Phi \quad \bar{\mathbf{f}}(t) = \mathbf{W}\Phi^+\mathbf{f} \quad (22b)$$

<sup>190</sup> where  $\mathbf{W} \in \mathbb{R}^{N \times N}$  is a diagonal matrix with the  $i$ -th element as  $[\mathbf{W}]_{ii} = |\mathcal{V}_k|$  if  $i \in$   
<sup>191</sup>  $\mathcal{V}_k$ . As shown in the Appendix, the examination of the second residual term  $\mathbf{r}^{(2)}(\mathbf{u}, t)$  in  
<sup>192</sup> eq. (20) reveals the physical sources of missing dynamics in the LCM: the approximation of  
<sup>193</sup> non-uniform temperature within each component as a constant, and the elimination of the  
<sup>194</sup> advection term due to coarse-graining.

<sup>195</sup> In sum, the above results not only show that the LCM is a result of coarse-graining of

<sup>196</sup> the full-order DG-FEM, but also reveal the discrepancies between the LCM and the DG-  
<sup>197</sup> FEM. In the subsequent section, the discrepancies will be corrected to produce the proposed  
<sup>198</sup> PIROM.

### <sup>199</sup> 3.2 Formulation of Reduced-Order Model

<sup>200</sup> The Mori-Zwanzig (MZ) formalism is an operator-projection technique used to derive ROMs  
<sup>201</sup> for high-dimensional dynamical systems, especially in statistical mechanics and fluid dynam-  
<sup>202</sup> ics Parish,Duraisamy . It provides an exact reformulation of the full-order dynamics in terms  
<sup>203</sup> of a subset of resolved variables. The proposed ROM is subsequently developed based on  
<sup>204</sup> such reformulation. Equation eq. (20) shows that the DG-FEM dynamics can be decomposed  
<sup>205</sup> into the resolved dynamics  $\mathbf{r}^{(1)}(\mathbf{u}, t)$  and the orthogonal dynamics  $\mathbf{r}^{(2)}(\mathbf{u}, t)$ , in the sense of  
<sup>206</sup>  $\mathcal{P}\mathbf{r}^{(2)} = 0$ . In this case, the MZ formalism can be invoked to express the dynamics  $\dot{\bar{\mathbf{u}}}$  in terms  
<sup>207</sup> of  $\bar{\mathbf{u}}$  alone as the projected Generalized Langevin Equation (GLE) Parish,Duraisamy ,

$$\dot{\bar{\mathbf{u}}}(t) = \mathbf{r}^{(1)}(\bar{\mathbf{u}}, t) + \int_0^t \tilde{\boldsymbol{\kappa}}(t, s, \bar{\mathbf{u}}) ds \quad (23)$$

<sup>208</sup> where the first term is Markovian, and the integral term is referred to as the memory. The  
<sup>209</sup> integral term is non-Markovian, accounting for impact of past resolved states on the current  
<sup>210</sup> states through their interactions with the un-resolved states.

<sup>211</sup> Next, to further inform the subsequent derivation of the ROM, the kernel  $\tilde{\mathbf{k}}$  is examined  
<sup>212</sup> via a leading-order expansion, based on prior work x; this can be viewed as an analog of  
<sup>213</sup> zeroth-order holding in linear system theory with a sufficiently small time step. In this case,  
<sup>214</sup> the memory kernel is approximated as,

$$\tilde{\boldsymbol{\kappa}}(t, s, \bar{\mathbf{u}}) \approx \mathbf{r}^{(1)}(\bar{\mathbf{u}}, t) \cdot \nabla_{\bar{\mathbf{u}}} \mathbf{r}^{(2)}(\Phi \bar{\mathbf{u}}, t) \quad (24)$$

<sup>215</sup> Note that the terms in  $\mathbf{r}^{(1)}$  have a common factor  $\bar{\mathbf{A}}^{-1}$ ; this motivates the following heuristic  
<sup>216</sup> modification of the model form in eq. (23),

$$\dot{\bar{\mathbf{u}}} = \mathbf{r}^{(1)}(\bar{\mathbf{u}}, t) + \bar{\mathbf{A}}^{-1}(\bar{\mathbf{u}}) \int_0^t \boldsymbol{\kappa}(t, s, \bar{\mathbf{u}}) ds \quad (25a)$$

$$\bar{\mathbf{A}}(\bar{\mathbf{u}})\dot{\bar{\mathbf{u}}} = \bar{\mathbf{B}}(\bar{\mathbf{u}})\bar{\mathbf{u}} + \bar{\mathbf{f}}(t) + \int_0^t \boldsymbol{\kappa}(t, s, \bar{\mathbf{u}}) ds \quad (25b)$$

<sup>217</sup> where the original kernel  $\tilde{\boldsymbol{\kappa}}$  is effectively normalized by  $\bar{\mathbf{A}}^{-1}$ . Intuitively, such choice of kernel  
<sup>218</sup> reduces its dependency on the averaged material properties, and simplifies the subsequent  
<sup>219</sup> design of model form.

220 Subsequently, the hidden states are introduced to “Markovianize” the system eq. (23).  
 221 In this manner, eq. (25b) is converted into a pure state-space model, with the functional  
 222 form of the LCM retained; since LCM is a physics-based model, then it encodes the phys-  
 223 ical information and retains explicit parametric dependence of the problem. Consider the  
 224 representation of the kernel as a finite sum of simpler functions, e.g., exponentials,

$$\kappa(t, s, \bar{\mathbf{u}}) = \sum_{j=1}^m \mathcal{K}_j(t, s, \bar{\mathbf{u}}) [\mathbf{p}_j + \mathbf{d}_j(\bar{\mathbf{u}})] \phi_j(s, \bar{\mathbf{u}}) \quad (26)$$

225 where,

$$\mathcal{K}_j(t, s, \bar{\mathbf{u}}) = e^{-\int_s^t (\lambda_j + e_j(\bar{\mathbf{u}})) d\tau}, \quad \phi_j(s, \bar{\mathbf{u}}) = \mathbf{q}_j^\top \bar{\mathbf{u}}(s) + \mathbf{g}_j(\bar{\mathbf{u}})^\top \bar{\mathbf{u}}(s) + \mathbf{r}_j^\top \bar{\mathbf{f}}(s) \quad (27)$$

226 with suitable coefficients  $\mathbf{p}_j, \mathbf{d}_j, \mathbf{q}_j, \mathbf{g}_j, \mathbf{r}_j \in \mathbb{R}^N$  and decay rates  $\lambda_j, e_j(\bar{\mathbf{u}}) > 0$ , that need to  
 227 be identified from data.

228 Define the hidden states as,

$$\beta_j(t) = \int_0^t \mathcal{K}_j(s, \bar{\mathbf{u}}) \phi_j(s, \bar{\mathbf{u}}) ds \quad (28)$$

229 then through its differentiation with respect to time,

$$\dot{\beta}_j(t) = -[\lambda_j + e_j(\bar{\mathbf{u}})] \beta_j(t) + \mathbf{q}_j^\top \bar{\mathbf{u}}(t) + \mathbf{g}_j(\bar{\mathbf{u}})^\top \bar{\mathbf{u}}(t) + \mathbf{r}_j^\top \bar{\mathbf{f}}(t) \quad (29)$$

230 and the memory term becomes,

$$\int_0^t \kappa(t, s, \bar{\mathbf{u}}) ds = \sum_{j=1}^m [\mathbf{p}_j + \mathbf{d}_j(\bar{\mathbf{u}})] \beta_j(t) \quad (30)$$

231 Then, eq. (25b) is recast as the extended Markovian system,

$$\bar{\mathbf{A}}(\bar{\mathbf{u}}) \dot{\bar{\mathbf{u}}} = \bar{\mathbf{B}}(\bar{\mathbf{u}}) \bar{\mathbf{u}} + [\mathbf{P} + \mathbf{D}(\bar{\mathbf{u}})] \boldsymbol{\beta} + \bar{\mathbf{f}}(t) \quad (31a)$$

$$\dot{\boldsymbol{\beta}} = [-\boldsymbol{\Lambda} + \mathbf{E}(\bar{\mathbf{u}})] \boldsymbol{\beta} + [\mathbf{Q} + \mathbf{G}(\bar{\mathbf{u}})] \bar{\mathbf{u}} + \mathbf{R} \bar{\mathbf{f}}(t) \quad (31b)$$

<sup>232</sup> where,

$$\boldsymbol{\Lambda} = \text{diag}(\lambda_1, \lambda_2, \dots, \lambda_m) \in \mathbb{R}^{m \times m}, \quad \mathbf{P} = [\mathbf{p}_1, \mathbf{p}_2, \dots, \mathbf{p}_m] \in \mathbb{R}^{N \times m} \quad (32a)$$

$$\mathbf{D}(\bar{\mathbf{u}}) = [\mathbf{d}_1(\bar{\mathbf{u}}), \mathbf{d}_2(\bar{\mathbf{u}}), \dots, \mathbf{d}_m(\bar{\mathbf{u}})] \in \mathbb{R}^{N \times m}, \quad \mathbf{Q} = [\mathbf{q}_1, \mathbf{q}_2, \dots, \mathbf{q}_m] \in \mathbb{R}^{m \times N} \quad (32b)$$

$$\mathbf{G}(\bar{\mathbf{u}}) = [\mathbf{g}_1(\bar{\mathbf{u}}), \mathbf{g}_2(\bar{\mathbf{u}}), \dots, \mathbf{g}_m(\bar{\mathbf{u}})] \in \mathbb{R}^{m \times N}, \quad \mathbf{R} = [\mathbf{r}_1, \mathbf{r}_2, \dots, \mathbf{r}_m] \in \mathbb{R}^{m \times N} \quad (32c)$$

$$\mathbf{E}(\bar{\mathbf{u}}) = \text{diag}(e_1(\bar{\mathbf{u}}), e_2(\bar{\mathbf{u}}), \dots, e_m(\bar{\mathbf{u}})) \in \mathbb{R}^{m \times m} \quad (32d)$$

<sup>233</sup> Since the hidden states  $\boldsymbol{\beta}$  serve as the memory, their initial conditions are set to zero, i.e.,  
<sup>234</sup>  $\boldsymbol{\beta}(t_0) = \mathbf{0}$ , no memory at the beginning. The physics-infused model in eq. (31) retains the  
<sup>235</sup> structure of the LCM, while the hidden states account for missing physics through corrections  
<sup>236</sup> to the stiffness and advection matrices, as well as the forcing term.

<sup>237</sup> Lastly, denote the collection of resolved and hidden states as  $\mathbf{y} = [\bar{\mathbf{u}}, \boldsymbol{\beta}]^T \in \mathbb{R}^{n_y}$  with  
<sup>238</sup>  $n_y = N + m$ , then the proposed PIROM is summarized as,

$$\tilde{\mathbf{A}}\dot{\mathbf{y}} = [\tilde{\mathbf{B}} + \tilde{\mathbf{C}}] \mathbf{y} + \mathbf{H}\bar{\mathbf{f}}(t) \quad (33a)$$

$$\mathbf{z} = \mathbf{M}\mathbf{y} \quad (33b)$$

<sup>239</sup> where,

$$\tilde{\mathbf{A}} = \begin{bmatrix} \bar{\mathbf{A}}(\bar{\mathbf{u}}) & \mathbf{O} \\ \mathbf{O} & \mathbf{I} \end{bmatrix} \in \mathbb{R}^{n_y \times n_y}, \quad \tilde{\mathbf{B}} = \begin{bmatrix} \bar{\mathbf{B}}(\bar{\mathbf{u}}) & \mathbf{P} \\ \mathbf{Q} & -\boldsymbol{\Lambda} \end{bmatrix} \in \mathbb{R}^{n_y \times n_y}, \quad \tilde{\mathbf{C}} = \begin{bmatrix} \mathbf{0} & \mathbf{D}(\bar{\mathbf{u}}) \\ \mathbf{G}(\bar{\mathbf{u}}) & \mathbf{E}(\bar{\mathbf{u}}) \end{bmatrix} \in \mathbb{R}^{n_y \times n_y}, \quad (34a)$$

$$\mathbf{H} = \begin{bmatrix} \mathbf{I} \\ \mathbf{R} \end{bmatrix} \in \mathbb{R}^{n_y \times N}, \quad \mathbf{M} \in \mathbb{R}^{n_z \times n_y} \quad (34b)$$

<sup>240</sup> In eq. (33), the terms  $\bar{\mathbf{A}}$ ,  $\bar{\mathbf{B}}$ , and  $\bar{\mathbf{f}}$  are the LCM terms. The collection of matrices,

$$\boldsymbol{\Theta} = \{\mathbf{P}, \mathbf{D}(\bar{\mathbf{u}}), \mathbf{G}(\bar{\mathbf{u}}), \boldsymbol{\Lambda}, \mathbf{E}(\bar{\mathbf{u}}), \mathbf{Q}, \mathbf{G}(\bar{\mathbf{u}}), \mathbf{R}, \mathbf{M}\} \in \mathbb{R}^{n_\theta} \quad (35)$$

<sup>241</sup> are learnable parameters to capture the memory effects. Particularly, the matrices  $\mathbf{P}$ ,  $\boldsymbol{\Lambda}$ ,  $\mathbf{Q}$ ,  $\mathbf{R}$   
<sup>242</sup> are constants that need to be identified from data, and account for the effects of coarse-  
<sup>243</sup> graining on the stiffness and forcing matrices. The matrices  $\mathbf{D}(\bar{\mathbf{u}})$ ,  $\mathbf{E}(\bar{\mathbf{u}})$ ,  $\mathbf{G}(\bar{\mathbf{u}})$  are state-  
<sup>244</sup> dependent matrices, and account for the effects of coarse-graining on the advection matrix.  
<sup>245</sup> Leveraging the DG-FEM formula for the advection matrix in eq. (44c) in the Appendix, and  
<sup>246</sup> noting that the mesh displacements are functions of the ablating velocity as in eq. (3), the

<sup>247</sup> state-dependent matrices for the  $i$ -th component are written as,

$$\mathbf{D}^{(i)}(\bar{\mathbf{u}}) \approx f^{(i)}(\bar{u}^{(i)})\mathbf{D}^{(i)}, \quad \mathbf{E}^{(i)}(\bar{\mathbf{u}}) \approx f^{(i)}(\bar{u}^{(i)})\mathbf{E}^{(i)}, \quad \mathbf{G}^{(i)}(\bar{\mathbf{u}}) \approx f^{(i)}(\bar{u}^{(i)})\mathbf{G}^{(i)} \quad (36)$$

<sup>248</sup> where  $f^{(i)}(\bar{u}^{(i)})$  is the surface recession velocity function in eq. (12) for the  $i$ -th component,  
<sup>249</sup> and  $\mathbf{D}^{(i)}, \mathbf{E}^{(i)}, \mathbf{G}^{(i)}$  are constant matrices to be identified from data. In eq. (33),  $\mathbf{M}$  is a  
<sup>250</sup> fully-populated matrix that extracts the observables, i.e., the surface temperatures, from  
<sup>251</sup> the PIROM states  $\mathbf{y}$ . The PIROM incorporates explicit information on the temperature-  
<sup>252</sup> dependent material properties through the LCM matrices, as well as the surface recession  
<sup>253</sup> velocity function through eq. (36). The next step is focused on identifying the unknown  
<sup>254</sup> parameters  $\Theta$  characterizing the hidden dynamics.

### <sup>255</sup> 3.3 Learning the Hidden Dynamics from Data

<sup>256</sup> The learning of the PIROM is achieved through a neural-ODE like approach [Chen2018](#).  
<sup>257</sup> For ease of presentation, consider the following compact form of the PIROM in eq. (33),

$$\mathcal{F}(\dot{\mathbf{y}}, \mathbf{y}; \boldsymbol{\xi}, \Theta) = \mathbf{0} \quad (37)$$

<sup>258</sup> where  $\boldsymbol{\xi}$  defines the parametrization of the problem, i.e., operating conditions, such as the  
<sup>259</sup> BC's, as well as the material properties. Consider a dataset of  $N_s$  high-fidelity trajectories  
<sup>260</sup> of observables over a time interval  $[t_0, t_f]$ ,

$$\mathcal{D} = \left\{ \left( t_k, \mathbf{z}_{\text{HF}}^{(l)}(t_k), \boldsymbol{\xi}^{(l)} \right) \right\}_{l=1}^{N_s}, \quad k = 0, 1, \dots, K \quad (38)$$

<sup>261</sup> The learning problem is formulated as the following differentially-constrained problem,

$$\min_{\Theta} \quad \frac{1}{N_s} \sum_{l=1}^{N_s} \frac{1}{K} \sum_{k=0}^K \left\| \mathbf{z}_{\text{HF}}^{(l)}(t_k) - \mathbf{M}\mathbf{y}^{(l)}(t_k) \right\|_2^2 \quad (39a)$$

$$\text{s.t.} \quad \mathcal{F}(\dot{\mathbf{y}}^{(l)}, \mathbf{y}^{(l)}; \boldsymbol{\xi}^{(l)}, \Theta) = \mathbf{0}, \quad t \in [t_0, t_f], \quad l = 1, 2, \dots, N_s \quad (39b)$$

$$\mathbf{y}^{(l)}(t_0) = \mathbf{y}_0(\boldsymbol{\xi}^{(l)}), \quad l = 1, 2, \dots, N_s \quad (39c)$$

262 **A Technical Details**

263 This appendix presents the technical details of the PIROM framework applied to the TPS  
264 ablation problem. The first section provides the mathematical details for the definition of  
265 the DG-FEM. The second section follows the projection procedures from Ref. x, and demon-  
266 strates the effects of coarse-graining on the advection matrix. The third section presents the  
267 derivation of the LCM model from an energy-conservation perspective.

268 **A.1 Full-Order Model**

269 To obtain the full-order numerical solution, the governing equation is spatially discretized  
270 using variational principles of Discontinuous Galerkin (DG) to result in a high-dimensional  
271 system of ordinary differential equations (ODEs). The DG-FEM model is written in an  
272 element-wise form, which is beneficial for subsequent derivations of the lower-order models.  
273 Note that the choice of DG approach here is mainly for theoretical convenience in the sub-  
274 sequent coarse-graining formulation. In the numerical results, the full-order TPS ablation  
275 simulations is computed using standard FEM instead, and the equivalence between DG and  
276 standard FEM is noted upon their convergence.

277 **A.1.1 Domain Discretization**

278 Consider a conforming mesh partition of the domain, as shown in Fig. DOMAIN, where each  
279 element belongs to one and only one component. Denote the collection of all  $M$  elements  
280 as  $\{E_i\}_{i=1}^M$ . To ease the description of the DG model, a graph structure is employed. The  
281 elements are treated as vertices, the set of which is denoted  $\mathcal{V} = \{m\}_{m=1}^M$ . Two neighboring  
282 elements,  $E_i$  and  $E_j$ , are connected by an edge  $(i, j)$ , and the shared boundary between them  
283 is denoted  $e_{ij}$ . The collection of all edges are denoted  $\mathcal{E}$ , and  $\mathcal{G}$  is referred to as a graph.  
284 In the graph, the edges are unidirected, meaning if  $(i, j) \in \mathcal{E}$  then  $(j, i) \in \mathcal{E}$ . Furthermore,  
285 denote the neighbors of the  $i$ -th element as  $\mathcal{N}_i = \{j | (i, j) \in \mathcal{E}\}$ . Lastly, for the ease of  
286 notation, introduce two special indices:  $T$  for the boundary of an element that overlaps with  
287 the Dirichlet boundary condition, and similarly  $q$  for the Neumann boundary condition.

288 **A.1.2 Weak Form of Discontinuous Galerkin Method**

289 Choosing appropriate basis functions  $\phi_k$  and  $\phi_l$  and using the Interior Penalty Galerkin  
290 (IPG) scheme [?], the variational bilinear form for eq. (1a) is,

$$\sum_{i=1}^M a_{\epsilon,i}(\phi_k, \phi_l) = \sum_{i=1}^M L_i(\phi_k) \quad (40)$$

291 where  $\epsilon$  is an user-specified parameter and,

$$a_{\epsilon,i}(\phi_k, \phi_l) = \int_{E^{(i)}} \left( \rho c_p \phi_k \frac{\partial \phi_l}{\partial t} + \nabla \phi_k \cdot (\mathbf{k} \nabla \phi_l) - \rho c_p \phi_k \mathbf{v} \cdot \nabla \phi_l \right) dE^{(i)} \quad (41a)$$

$$\begin{aligned} &= - \sum_{j \in \mathcal{N}_i \cup \{T_b\}} \int_{e_{ij}} \{ \mathbf{k} \nabla \phi_k \cdot n \} [\phi_l] de_{ij} + \epsilon \sum_{j \in \mathcal{N}_i \cup \{T_b\}} \int_{e_{ij}} \{ \mathbf{k} \nabla \phi_l \cdot n \} [\phi_k] de_{ij} \\ &\quad + \sigma \sum_{j \in \mathcal{N}_i \cup \{T_b\}} \int_{e_{ij}} [\phi_k] [\phi_l] de_{ij} \end{aligned} \quad (41b)$$

$$L_i(v) = \epsilon \sum_{j \in \mathcal{N}_i \cup \{T_b\}} \int_{e_{ij}} (\mathbf{k} \nabla \phi_l \cdot n) T_b de_{ij} + \int_{e_{iq}} \phi_k q_b de_{iq} + \sigma \int_{e_{iT}} \phi_k T_b de_{iT} \quad (41c)$$

292 In the bi-linear form above, the notations  $[]$  and  $\{\}$  are respectively the jumps and averages  
293 at the boundary  $e_{ij}$  share by two elements  $E_i$  and  $E_j$ ,

$$[u] = u|_{E_i} - u|_{E_j}, \quad \{u\} = \frac{1}{2} \left( u|_{E_i} + u|_{E_j} \right), \quad \text{for } x \in e_{ij} = E_i \cap E_j$$

294 Furthermore, in the bi-linear form, the terms associated with  $\sigma$  are introduced to enforce  
295 the Dirichlet boundary conditions;  $\sigma$  is a penalty factor whose value can depend on the size  
296 of an element. Depending on the choice of  $\epsilon$ , the bi-linear form corresponds to symmetric  
297 IPG ( $\epsilon = -1$ ), non-symmetric IPG ( $\epsilon = 1$ ), and incomplete IPG ( $\epsilon = 0$ ). All these schemes  
298 are consistent with the original PDE and have similar convergence rate with respect to mesh  
299 size. In the following derivations, the case  $\epsilon = 0$  is chosen for the sake of simplicity.

300 **A.1.3 Discontinuous Galerkin Model**

301 Next, the DG-based model is written in an element-wise form. For the  $i$ -th element, use a  
302 set of  $P$  trial functions to represent the temperature as in eq. (5). Without loss of generality,  
303 the trial functions are assumed to be orthogonal, so that  $\int_{E^{(i)}} \phi_k^{(i)}(x) \phi_l^{(i)}(x) dx = |E^{(i)}| \delta_{kl}$ ,  
304 where  $|E^{(i)}|$  is the area ( $n_d = 2$ ) or volume ( $n_d = 3$ ) of the  $i$ -th element, and  $\delta_{kl}$  is the  
305 Kronecker delta.

306 Using test functions same as trial functions, the dynamics  $\mathbf{u}^{(i)}$  is obtained by evaluating

<sup>307</sup> the element-wise bi-linear forms,

$$a_{\epsilon,i}(\phi_k^{(i)}, T^{(i)}) = L_i(\phi_k^{(i)}), \quad k = 1, 2, \dots, P \quad (42)$$

<sup>308</sup> The above procedure yields,

$$\mathbf{A}^{(i)} \dot{\mathbf{u}}^{(i)} = (\mathbf{B}^{(i)} + \mathbf{C}^{(i)}(t)) \mathbf{u}^{(i)} + \sum_{j \in \mathcal{N}_i \cup \{T_b\}} \left( \mathbf{B}_{ij}^{(i)} \mathbf{u}^{(i)} + \mathbf{B}_{ij}^{(j)} \mathbf{u}^{(j)} \right) + \mathbf{f}^{(i)}(t) \quad (43)$$

<sup>309</sup> where for  $k, l = 1, 2, \dots, P$ ,

$$[\mathbf{A}^{(i)}]_{kl} = \int_{E^{(i)}} \rho c_p \phi_k^{(i)} \phi_l^{(i)} dE^{(i)} \quad (44a)$$

$$[\mathbf{B}^{(i)}]_{kl} = - \int_{E^{(i)}} (\nabla \phi_k^{(i)}) \cdot (\mathbf{k} \nabla \phi_l^{(i)}) dE^{(i)} \quad (44b)$$

$$[\mathbf{C}^{(i)}]_{kl} = \int_{E^{(i)}} \rho c_p \phi_k^{(i)} \mathbf{v}^{(i)} \cdot \nabla \phi_l^{(i)} dE^{(i)} \quad (44c)$$

$$[\mathbf{B}_{ij}^{(i)}] = \int_{e_{ij}} \left\{ \mathbf{k} \nabla \phi_k^{(i)} \cdot \hat{n} \right\} \phi_l^{(i)} - \sigma [\phi_k^{(i)}] \phi_l^{(i)} de_{ij} \quad (44d)$$

$$[\mathbf{B}_{ij}^{(j)}] = \int_{e_{ij}} - \left\{ \mathbf{k} \nabla \phi_k^{(i)} \cdot \hat{n} \right\} \phi_l^{(j)} + \sigma [\phi_k^{(i)}] \phi_l^{(j)} de_{ij} \quad (44e)$$

$$[\mathbf{f}^{(i)}]_k = \int_{e_{iq}} \phi_k^{(i)} q_b de_{iq} + \sigma \int_{e_{iT}} \phi_k^{(i)} de_{iT} \quad (44f)$$

<sup>310</sup> The matrices  $\mathbf{A}^{(i)} \in \mathbb{R}^{P \times P}$ ,  $\mathbf{B}^{(i)} \in \mathbb{R}^{P \times P}$ , and  $\mathbf{C}^{(i)} \in \mathbb{R}^{P \times P}$  are respectively the capacitance,  
<sup>311</sup> conductivity, and advection matrices for element  $i$ . These matrices depend on  $\rho$ ,  $c_p$ ,  $\mathbf{k}$ , and  
<sup>312</sup>  $\mathbf{v}$ , and hence can be non-linear functions of  $\mathbf{u}^{(i)}$ . Since the trial functions are orthogonal, if  
<sup>313</sup>  $\rho c_p$  is constant within an element,  $\mathbf{A}^{(i)}$  is diagonal; otherwise,  $\mathbf{A}_i$  is symmetric and positive  
<sup>314</sup> definite as  $\rho c_p > 0$ .

<sup>315</sup> For compactness, the element-wise model in eq. (43) is also written in matrix form,

$$\mathbf{A}(\dot{\mathbf{u}}) = [\mathbf{B}(\mathbf{u}) + \mathbf{C}(\mathbf{u})] \mathbf{u} + \mathbf{f}(t) \quad (45)$$

<sup>316</sup> where  $\mathbf{u} = [\mathbf{u}^{(1)}, \mathbf{u}^{(2)}, \dots, \mathbf{u}^{(M)}]^T \in \mathbb{R}^{MP}$  includes all DG variables,  $\mathbf{f} = [\mathbf{f}^{(1)}, \mathbf{f}^{(2)}, \dots, \mathbf{f}^{(M)}]^T \in \mathbb{R}^{MP}$ ,  $\mathbf{A}$  and  $\mathbf{C}$  are matrices of  $M$  diagonal blocks whose  $i$ -th blocks are  $\mathbf{A}^{(i)}$  and  $\mathbf{C}^{(i)}$ , and  
<sup>317</sup>  $\mathbf{B}$  is a matrix of  $M \times M$  blocks whose  $(i, j)$ -th block is,  
<sup>318</sup>

$$\mathbf{B}_{ij} = \begin{cases} \mathbf{B}^{(i)} + \sum_{j \in \mathcal{N}_i \cup \{T_b\}} \mathbf{B}_{ij}^{(i)}, & i = j \\ \mathbf{B}_{ij}^{(j)}, & i \neq j \end{cases} \quad (46)$$

319 The dependency of  $\mathbf{A}$ ,  $\mathbf{B}$ , and  $\mathbf{C}$  on  $\mathbf{u}$  is explicitly noted in eq. (45), which is the source of  
320 non-linearity in the current TPS problem. Moreover, the mesh velocity  $\mathbf{v}$  varies with space  
321 and time, and thus the advection matrix  $\mathbf{C}$  varies with time as a function of  $q_b$ .

## 322 A.2 Coarse-Graining of Dynamics

323 The LCM is obtained by coarse-graining the full-order DG-FEM. This coarse-graining proce-  
324 dure produces resolved  $\mathbf{r}^{(1)}(\mathbf{u}, t)$  and residual  $\mathbf{r}^{(2)}(\mathbf{u}, t)$  dynamics as in eq. (20). This section  
325 presents the detail derivations and magnitude analysis for the resolved and residual dynam-  
326 ics.

### 327 A.2.1 Resolved Dynamics

328 Using eq. (17), the resolved dynamics is computed as follows,

$$\mathbf{r}^{(1)}(\mathbf{u}, t) = \mathcal{P} [\Phi^+ \mathbf{A}(\mathbf{u})^{-1} (\mathbf{B}(\mathbf{u})\mathbf{u} + \mathbf{C}(\mathbf{u})\mathbf{u} + \mathbf{f}(t))] \quad (47a)$$

$$\begin{aligned} &= \Phi^+ \mathbf{A}(\mathbf{Pu})^{-1} \mathbf{PB}(\mathbf{Pu}) \mathbf{Pu} + \Phi^+ \mathbf{A}(\mathbf{Pu})^{-1} \mathbf{PC}(\mathbf{Pu}) \mathbf{Pu} \\ &\quad + \Phi^+ \mathbf{A}(\mathbf{Pu})^{-1} \mathbf{Pf}(t, \mathbf{Pu}) \end{aligned} \quad (47b)$$

$$\begin{aligned} &= \underbrace{\Phi^+ \mathbf{A}(\Phi \bar{\mathbf{u}})^{-1} \Phi}_{\#1} \underbrace{\Phi^+ \mathbf{B}(\Phi \bar{\mathbf{u}}) \Phi \bar{\mathbf{u}}}_{\#2} + \Phi^+ \mathbf{A}(\Phi \bar{\mathbf{u}})^{-1} \Phi \underbrace{\Phi^+ \mathbf{C}(\Phi \bar{\mathbf{u}}) \Phi \bar{\mathbf{u}}}_{\#3} \\ &\quad + \Phi^+ \mathbf{A}(\Phi \bar{\mathbf{u}})^{-1} \Phi \underbrace{\Phi^+ \mathbf{f}(t, \Phi \bar{\mathbf{u}})}_{\#4} \end{aligned} \quad (47c)$$

329 Detailed derivations for the #1, #2, and #4 terms can be found in Ref. [x](#). The effects of  
330 coarse-graining on the advection term #3 are analyzed next.

331 **Term #3** The  $\mathbf{C}(\mathbf{u}) \in \mathbb{R}^{MP \times MP}$  matrix contains  $M$  diagonal of size  $P \times P$ , since the  
332 basis functions are defined locally on each element. Therefore,  $[\mathbf{C}(\mathbf{u})]_{ij} = \mathbf{0}$  for all  $i \neq j$  with  
333  $i, j = 1, 2, \dots, M$ . It follows that for  $k, l = 1, 2, \dots, N$ ,

$$[\Phi^+ \mathbf{C}(t, \Phi \bar{\mathbf{u}}) \Phi]_{kl} = \sum_{i=1}^M \sum_{j=1}^M \boldsymbol{\varphi}_i^{k+} [\mathbf{C}(t, \Phi \bar{\mathbf{u}})]_{ij} \boldsymbol{\varphi}_j^l \quad (48a)$$

$$= \sum_{i=1}^M \boldsymbol{\varphi}_i^{k+} [\mathbf{C}(t, \Phi \bar{\mathbf{u}})]_{ii} \boldsymbol{\varphi}_i^l \quad (48b)$$

$$= \sum_{i \in \mathcal{V}_k} \boldsymbol{\varphi}_i^{k+} [\mathbf{C}(t, \Phi \bar{\mathbf{u}})]_{ii} \boldsymbol{\varphi}_i^l \quad (48c)$$

<sup>334</sup> where in the second row, the fact that  $[\mathbf{C}(\mathbf{u})]_{ij} = 0$  for all  $i \neq j$  is used, and in the last row,  
<sup>335</sup> the fact that  $\varphi_i^{k+} = 0$  for all  $i \notin \mathcal{V}_k$  is used. Now, considering that  $[\mathbf{C}(\mathbf{u})]_{ii}$  has a  $(1, 1)$ -th  
<sup>336</sup> zero element, i.e.,  $[C_{11}(t, \Phi\bar{\mathbf{u}})]_{ii} = 0$ , and that if  $k \neq l$  then  $i \notin \mathcal{V}_l$  and thus  $\varphi_i^l = \mathbf{0}$ , it follows  
<sup>337</sup> that for some index  $i \in \mathcal{V}_k$ ,

$$\varphi_i^{k+} [\mathbf{C}(t, \Phi\bar{\mathbf{u}})]_{ii} \varphi_i^l = \varphi_i^{k+} [\mathbf{C}(t, \Phi\bar{\mathbf{u}})]_{ii} \varphi_i^k = \frac{|E_i|}{|\Omega_k|} [C_{11}(t, \Phi\bar{\mathbf{u}})]_{ii} = 0 \quad (49)$$

<sup>338</sup> The matrix  $[\Phi^+ \mathbf{C}(t, \Phi\bar{\mathbf{u}}) \Phi]_{kl} = 0$  for all  $k, l = 1, 2, \dots, N$ , and thus,

$$\bar{\mathbf{C}}(t, \bar{\mathbf{u}}) = \Phi^+ \mathbf{C}(t, \Phi\bar{\mathbf{u}}) \Phi = \mathbf{0} \quad (50)$$

<sup>339</sup> as indicated by the LCM in eq. (8).

### <sup>340</sup> A.2.2 Magnitude Analysis for Residual Dynamics

<sup>341</sup> Next, the magnitude of the residual dynamics  $\mathbf{r}^{(2)}(\mathbf{u}, t)$  is analyzed to pinpoint the missing  
<sup>342</sup> physics in the LCM. By definition,

$$\mathbf{r}^{(2)}(\mathbf{u}, t) = \dot{\bar{\mathbf{u}}} - \mathbf{r}^{(1)}(\bar{\mathbf{u}}, t) \quad (51a)$$

$$= \Phi^+ \mathbf{r}(\mathbf{u}, t) - \mathbf{r}^{(1)}(\mathbf{u}, t) \quad (51b)$$

$$\begin{aligned} &= \underbrace{\Phi^+ \mathbf{A}(\mathbf{u})^{-1} \mathbf{B}(\mathbf{u}) \mathbf{u} - \bar{\mathbf{A}}(\bar{\mathbf{u}})^{-1} \bar{\mathbf{B}}(\bar{\mathbf{u}}) \bar{\mathbf{u}}}_{\#1} + \underbrace{\Phi^+ \mathbf{A}(\mathbf{u})^{-1} \mathbf{C}(\mathbf{u}) \mathbf{u} - \bar{\mathbf{A}}(\bar{\mathbf{u}})^{-1} \bar{\mathbf{C}}(t, \bar{\mathbf{u}}) \bar{\mathbf{u}}}_{\#2} \\ &\quad + \underbrace{\Phi^+ \mathbf{A}(\mathbf{u})^{-1} \mathbf{f}(t) - \bar{\mathbf{A}}(\bar{\mathbf{u}})^{-1} \bar{\mathbf{f}}(t)}_{\#3} \end{aligned} \quad (51c)$$

<sup>343</sup> The magnitude analysis for terms  $\#1$  and  $\#3$  can be found in Ref. [x](#). The analysis for term  
<sup>344</sup>  $\#2$  is presented next. Let  $\mathbf{D}(\bar{\mathbf{u}}) = \mathbf{A}(\Phi\bar{\mathbf{u}})^{-1} \mathbf{P} \mathbf{C}(t, \Phi\bar{\mathbf{u}})$ , then,

$$\Phi^+ \mathbf{A}(\mathbf{u})^{-1} \mathbf{C}(\mathbf{u}) \mathbf{u} - \bar{\mathbf{A}}(\bar{\mathbf{u}})^{-1} \bar{\mathbf{C}}(t, \bar{\mathbf{u}}) \bar{\mathbf{u}} \quad (52a)$$

$$= \Phi^+ \mathbf{A}(\mathbf{u})^{-1} \mathbf{C}(\mathbf{u}) \mathbf{u} - \Phi^+ \mathbf{A}(\Phi\bar{\mathbf{u}})^{-1} \mathbf{P} \mathbf{C}(t, \Phi\bar{\mathbf{u}}) \Phi \Phi^+ \mathbf{u} \quad (52b)$$

$$= \Phi^+ \mathbf{A}^{-1}(\mathbf{u}) \mathbf{C}(\mathbf{u}) \mathbf{u} - \Phi^+ \mathbf{D}(\bar{\mathbf{u}}) \Phi \Phi^+ \mathbf{u} \quad (52c)$$

$$(52d)$$

345 where  $\mathbf{P} = \Phi\Phi^+$ . Thus,

$$\|\Phi^+\mathbf{A}(\mathbf{u})^{-1}\mathbf{C}(\mathbf{u})\mathbf{u} - \bar{\mathbf{A}}^{-1}(\bar{\mathbf{u}})\bar{\mathbf{C}}(t, \bar{\mathbf{u}})\bar{\mathbf{u}}\| \quad (53a)$$

$$\leq \|\Phi^+\mathbf{A}^{-1}(\mathbf{u})\mathbf{C}(\mathbf{u})\mathbf{u} - \Phi^+\mathbf{D}(\bar{\mathbf{u}})\mathbf{u}\| + \|\Phi^+\mathbf{D}(\bar{\mathbf{u}})\mathbf{u} - \Phi^+\mathbf{D}(\bar{\mathbf{u}})\Phi\Phi^+\mathbf{u}\| \quad (53b)$$

$$\leq \|\Phi^+\| \underbrace{\|\mathbf{A}^{-1}(\mathbf{u})\mathbf{C}(\mathbf{u})\mathbf{u} - \mathbf{D}(\bar{\mathbf{u}})\mathbf{u}\|}_{\#1} + \|\Phi^+\mathbf{D}(\bar{\mathbf{u}})\| \underbrace{\|\mathbf{u} - \Phi\Phi^+\mathbf{u}\|}_{\#2} \quad (53c)$$

346 where term  $\#2$  is due to the appriximation of non-uniform temperaeture as constants, and  
 347 term  $\#1$  is the error in the advection dynamics due to coarse-graining.

### 348 A.3 Lumped Capacitance Model

349 The following assumptions are employed: (1) the temperature in component  $(i)$  is described  
 350 by a scalar time-varying average temperature  $\bar{u}^{(i)}$ , (2) between neighboring components  $(i)$   
 351 and  $(j)$  the heat flux is approximated as,

$$q_{ij} = \frac{\bar{u}^{(j)} - \bar{u}^{(i)}}{R_{ij}} \quad (54)$$

352 where  $R_{ij}$  is the thermal resistance. Empirically, for a component of isotropic heat conduc-  
 353 tivity  $k$ , length  $\ell$ , and cross-section area  $A$ , the thermal resistance is  $R = \ell/kA$ . Between  
 354 components  $i$  and  $j$ , define  $R_{ij} = R_i + R_j$ . In addition, the heat flux due to Dirichlet  
 355 boundary condition is computed as  $q_{iT} = (T_b - \bar{u}^{(i)})/R_i$ .

356 At component  $i$ , the dynamics of LCM are given by,

$$\int_{E^{(i)}} \rho c_p \dot{\bar{u}}^{(i)} dE^{(i)} = \left( \sum_{j \in \mathcal{N}_i} \int_{e_{ij}} \frac{\bar{u}^{(j)} - \bar{u}^{(i)}}{R_{ij}} de_{ij} \right) + \int_{e_{iq}} q_b de_{iq} + \int_{e_{iT}} \frac{T_b - \bar{u}^{(i)}}{R_i} de_{iT} \quad (55a)$$

$$\bar{A}^{(i)} \dot{\bar{u}}^{(i)} = \left( \sum_{j \in \mathcal{N}_i} \frac{|e_{ij}|}{R_{ij}} (\bar{u}^{(j)} - \bar{u}^{(i)}) \right) + |e_{iq}| \bar{q}^{(i)} + \frac{|e_{iT}|}{R_i} (\bar{T}^{(i)} - \bar{u}^{(i)}) \quad (55b)$$

$$= \sum_{j \in \mathcal{N}_i} \left( -\frac{|e_{ij}|}{R_{ij}} \bar{u}^{(i)} + \frac{|e_{ij}|}{R_{ij}} \bar{u}^{(j)} \right) + \left( -\frac{|e_{iT}|}{R_i} \bar{u}^{(i)} \right) + \left( |e_{iq}| \bar{q}^{(i)} + \frac{|e_{iT}|}{R_i} \bar{T}^{(i)} \right) \quad (55c)$$

$$= \sum_{j \in \mathcal{N}_i \cup \{T_b\}} \left( \bar{B}_{ij}^{(i)} \bar{u}^{(i)} + \bar{B}_{ij}^{(j)} \bar{u}^{(j)} \right) + \bar{f}^{(i)} \quad (55d)$$

357 where in eq. (55b)  $|e|$  denotes the length ( $d = 2$ ) or area ( $d = 3$ ) of a component boundary  
 358  $e$ . The  $\bar{A}^{(i)}$ ,  $\bar{B}_{ij}^{(i)}$ , and  $\bar{B}_{ij}^{(j)}$  quantities are provided in eq. (11).

359 The lumped-mass representation for the four-component TPS is shown in Fig. 2. Let  $v_i$

represent the area of the  $i$ -th element,  $\overline{\rho c_p}_{,i}$ , the heat capacity evaluated using the average temperature  $\bar{u}^{(i)}$ , and  $1/R_{ij} = 1/R_i(\bar{u}^{(i)}) + 1/R_j(\bar{u}^{(j)})$  the equivalent thermal resistance between elements  $i$  and  $j$ . Leveraging the formulas from eqs. (10) and (11), the LCM matrices are given by,

$$\bar{\mathbf{A}} = \begin{bmatrix} \overline{\rho c_p}_{,1} v_1 & 0 & 0 & 0 \\ 0 & \overline{\rho c_p}_{,2} v_2 & 0 & 0 \\ 0 & 0 & \overline{\rho c_p}_{,3} v_3 & 0 \\ 0 & 0 & 0 & \overline{\rho c_p}_{,4} v_4 \end{bmatrix}, \quad (56a)$$

$$\bar{\mathbf{B}} = \begin{bmatrix} \frac{1}{R_{12}} + \frac{1}{R_{14}} & -\frac{1}{R_{12}} & 0 & -\frac{1}{R_{14}} \\ -\frac{1}{R_{12}} & \frac{1}{R_{12}} + \frac{1}{R_{24}} + \frac{1}{R_{23}} & -\frac{1}{R_{23}} & -\frac{1}{R_{24}} \\ 0 & -\frac{1}{R_{32}} & \frac{1}{R_{32}} + \frac{1}{R_{34}} & -\frac{1}{R_{34}} \\ -\frac{1}{R_{14}} & -\frac{1}{R_{24}} & -\frac{1}{R_{34}} & \frac{1}{R_{14}} + \frac{1}{R_{24}} + \frac{1}{R_{34}} \end{bmatrix}, \quad \bar{\mathbf{f}} = \begin{bmatrix} \bar{q}^{(1)} \\ \bar{q}^{(2)} \\ \bar{q}^{(3)} \\ 0 \end{bmatrix} \quad (56b)$$